



HAL
open science

MgO monolayer epitaxy on Ni (100)

Brice Sarpi, Magali Putero, Anne Hémercyck, Sébastien Vizzini

► **To cite this version:**

Brice Sarpi, Magali Putero, Anne Hémercyck, Sébastien Vizzini. MgO monolayer epitaxy on Ni (100). Applied Physics Letters, 2017, 111 (21), pp.211604. 10.1063/1.5000119 . hal-01685588

HAL Id: hal-01685588

<https://hal.science/hal-01685588v1>

Submitted on 16 Jan 2018

HAL is a multi-disciplinary open access archive for the deposit and dissemination of scientific research documents, whether they are published or not. The documents may come from teaching and research institutions in France or abroad, or from public or private research centers.

L'archive ouverte pluridisciplinaire **HAL**, est destinée au dépôt et à la diffusion de documents scientifiques de niveau recherche, publiés ou non, émanant des établissements d'enseignement et de recherche français ou étrangers, des laboratoires publics ou privés.

MgO monolayer epitaxy on Ni (100)

B. Sarpi^a, M. Putero^b, A. Hemeryck^c and S. Vizzini^{b*}

^a*Synchrotron SOLEIL, l'Orme des Merisiers Saint-Aubin, 91192 Gif-sur-Yvette, France*

^b*Aix Marseille Université, IM2NP, Fac. Sci. St Jérôme, F-13397 Marseille cedex 20, France*

^c*LAAS CNRS, Université de Toulouse, CNRS, 31400 Toulouse, France*

Abstract: The growth of two-dimensional oxide films with accurate control of their structural and electronic properties is considered challenging for engineering nanotechnological applications. We address here the particular case of MgO ultrathin films grown on Ni (100), a system for which neither crystallization nor extended surface ordering have been established previously in the monolayer range. Using Scanning Tunneling Microscopy (STM) and Auger Electron Spectroscopy (AES), we report on experiments showing MgO monolayer (ML) epitaxy on a ferromagnetic nickel surface, down to the limit of atomic thickness. Alternate steps of Mg ML deposition, O₂ gas exposure, and ultrahigh vacuum (UHV) thermal treatment enable the production of a textured film of ordered MgO nano-domains. This study could open interesting prospects for controlled epitaxy of ultrathin oxide films with high magneto-resistance (MR) ratio on ferromagnetic substrates, enabling improvement in high-efficiency spintronics and magnetic tunnel junction devices.

Nowadays, oxide-based materials are widely used as building blocks materials in the process of engineering relevant technological applications, e.g. in catalysis, micro and nanoelectronics, sensoristics, spintronics, drug delivery, etc¹. Great research efforts have therefore been – and are still currently being – devoted to reach complete characterization of such oxides properties¹⁻⁹.

Ultrathin oxide films, when confined in the range of monolayer thicknesses, might exhibit an utmost interest among others. These oxides are known to show electronic and chemical characteristics different from those observed in the corresponding bulk materials, depending on films structure and defectivity^{1,6,10-12}. Low-dimensionality magnesium oxide has become the focus of intensive research in this field, mainly for its role as an interface material of great applicative potential¹³. Indeed, MgO has been explored as an high-k dielectric layer in electronic devices¹⁴ and more recently as an insulating tunnel barrier in magnetic tunnel junctions¹⁵. The epitaxy of the tunnel barrier is of crucial importance and may give rise to much higher tunneling spin polarization (TSP) and tunneling magnetoresistance (TMR) than those obtained with an amorphous tunnel barrier because of a highly spin-dependent evanescent decay of certain wave-functions, with particular transverse momentum values, across the tunnel barrier¹⁶. Crystalline MgO(100) spacer layers in magnetic tunnel junctions have attracted a lot of attention because of their high TMR values¹⁷ up to high theoretically MR ratio (1000%) predicted¹⁸, raising the great interest to elaborate controlled ultra-thin and crystalline oxide layer on ferromagnetic substrate.

Magnesium oxide deposition in thin films has been studied regarding a wide panel of metallic substrates in the literature¹⁹⁻¹⁹. On the other hand, few examples have successfully shown the epitaxy of thin oxide layers on Ni crystals, e.g. EuO / Ni(100)²⁰ and NiWO₄ / Ni(110)²¹. Jeong *et al.* have reported the growth of MgO on Ni particles by ALD²² in search of catalysis applications. Nevertheless, no study has been proposed for investigating the epitaxy of such oxide on nickel, neither in thin nor ultrathin films.

To tackle this challenge, previously our group has focused on developing an accurate MBE-based method^{23,24} for oxide films deposition in low-dimensions, that was tailored for studying MgO growth on diamagnetic metallic and semiconductor crystals^{25,26,27}. Following the same approach, we explore through this paper the first insights of epitaxial growth in the MgO ML / Ni (100) system, on the road towards two-dimensional crystallization.

All experiments presented in this study were performed *in-situ* in an UHV chamber housing Molecular Beam Epitaxy facilities and surface-sensitive analysis tools, i.e. Riber CMA Auger Electron Spectroscopy, Omicron Spectra Low Energy Electron Diffraction and Omicron Variable Temperature-Scanning Tunneling Microscopy.

The bare Ni(100) single-crystal was cleaned by repeated cycles of Ar⁺ sputtering (700eV) and annealing at 670K. This procedure resulted in extended atomic Ni terraces of high chemical cleanness probed with STM.

Magnesium oxide monolayer films were grown by using the three-step procedure described hereafter. One Mg monolayer (ML) was firstly deposited on the Ni(100) surface held at Room Temperature (RT), from a calibrated effusion cell in a background pressure of 2×10^{-10} Torr. Oxidation was then performed by exposing the Mg film to a constant pressure of molecular oxygen gas (10 Langmuirs) at RT. The (100)-textured MgO ML films were finally achieved through thermal activation processed under UHV at 720K for few minutes.

The calibration of the Mg deposition rate was defined using coupled AES and STM results discussed in the following. The AES plots presented in this work were obtained in the derivate mode by monitoring the Auger intensities of the metal Mg(LVV)_{45eV}, Ni(MVV)_{61eV}²⁸, O(KLL)_{51eV} and oxidized Mg(LVV)_{35eV}²⁹ low-energy transitions.

Figure 1(a) displays an AES experimental plot (black squares) showing evolution of the normalized peak to peak intensity of Ni_{61eV} as a function of magnesium deposition time. Regarding the exponential decay of the nickel signal, it is stated that magnesium grows in a *close to Frank van der Merwe fashion* at RT³⁰. Also, the close fitting between this AES plot and the theoretical curve of a layer-by-layer growth (red dots) highlights completion of the first monolayer after 4 seconds of Mg deposition, where the nickel peak is 63 % attenuated. Using AES attenuation equations tailored for this 2D growth^{31,32}, we assess formation of a magnesium monolayer being 2.88 Å thick, i.e. in the same order of magnitude as reports made on atomically thick Mg terraces³³.

Figure 1(b) shows a 400 x 400 nm² STM image recorded at the surface of the bare Ni(100), where four extended atomic steps can be observed. The nickel terraces appear here locally pinned with surface defects attributed to a residual contamination in carbon species. In **Figure 1(c)** the surface topography is depicted of a 250 x 250 nm² image probed after RT deposition of 1 Mg ML on the Ni growth template. This suggests, from a general perspective, a

mechanism of a monolayer completion taking place through the nucleation of disordered (i.e. amorphous) nanoscale features of Mg. In accordance with this apparently random distribution of the features in surface, no diffraction pattern could be probed afterwards for the deposited film under LEED observation. Taking a look at the corresponding line scan of **Figure 1(d)**, average width and height of 10 nm and 2 Å may be estimated for the Mg protrusions respectively. This reveals the growth of a discontinuous layer whose atomic thickness substantiates the AES attenuation of the Ni peak. **Consequently, the deposition of 1 Mg ML leads to the formation of a two-dimensional amorphous film that is dense enough for covering quite homogeneously the Ni terraces, and with a weak surface corrugation.**

In **Figure 2**, the evolution of the Mg, Ni and O Auger peak signals is monitored *in-situ* at each step of the oxide growth process, as detailed in the experimental section. The corresponding AES spectra were recorded by keeping the emission current at a constant value, to ensure qualitative analysis of the peaks intensity variations. On the first spectrum **(a)**, one can note a Ni_{61eV} Auger signal of high intensity for nickel and a weak peak of carbon contamination close to 273eV. This plot was used as a reference for studying the formation of the ultrathin MgO film. As the second spectrum **(b)** was monitored after RT deposition of 1 Mg ML, a pure signal of metallic magnesium appears at 45eV and contributes to a 68 % attenuation of the nickel peak intensity.

On the third spectrum **(c)** recorded after exposing the Mg ML to 10 Langmuirs of molecular oxygen at RT, a strong attenuation is observed for both the Mg and Ni signals, together with the O_{511eV} peak of oxygen adsorption. Also, an obvious energy shift of 10 eV is evidenced for the magnesium peak towards lower Auger energy values, which has been reported as a signature of Mg-O bonds formation³⁴. We emphasize that the RT oxidation does not affect the underlying nickel surface, keeping a characteristic signature of metal binding environment at Ni_{61 eV}. This addresses the potential role of oxygen diffusion barrier that might be played by the Mg ML deposited, in the sense that the Ni(100) surface remains un-oxidized during the RT process.

The atomic concentrations (given in at.%) of the chemical species present at the sample surface were quantified using the AES semi-quantitative equation that follows³⁵:

$$X_i = \frac{I_i}{S_i} \left(\sum_j \frac{I_j}{S_j} \right)^{-1}$$

where I_i and I_j represent the peak to peak intensities measured for the chemical compounds i and j respectively; S_i and S_j correspond to the AES sensitivity factors tabled in the Handbook of Auger Spectroscopy³⁵, i.e. 0.2 for Mg_{35eV}; 0.26 for Ni_{61eV} and 0.4 for O_{511eV}.

Regarding the peak intensities displayed on the oxidation spectrum, we estimate the surface atomic concentrations of Mg (29.9 at.%), O (31.2 at.%) and Ni (38.9 at.%) respectively. The ultrathin film formed therefore shows a chemical composition strongly consistent with the MgO stoichiometry, within the limits of AES sensitivity. Note that additional LEED investigations were conducted on the film obtained after RT oxidation (i.e. green AES spectrum). We concluded in an amorphous oxide growth at RT. Nevertheless, we underline such an AES signature of MgO compound reveals a stable oxide stoichiometry reached at room temperature. As the last spectrum **(d)** of Figure 2 was recorded after annealing of the sample at 720 K for few minutes, neither peak shift nor noticeable intensity variation could be

observed for the surface species. The MgO film therefore exhibits thermal stability within a wide range of processing temperatures, at least up to 720 K.

The influence of annealing with regard to the oxide structure was investigated afterwards under STM observation. Here again, **Figure 3(a)** displays a $400 \times 400 \text{ nm}^2$ image of the bare nickel used as a template for the oxide growth, showing locally carbon-induced surface defects. In a nearby probed sample region, **Figure 3(b)** presents a $400 \times 400 \text{ nm}^2$ area of the resulting oxide surface after processing few minutes of annealing at 720 K. As MgO-covered Ni(100), terraces and step edges can be solved at large scale in the image, this suggests a two-dimensional wetting of the Ni surface after annealing. With regard to the high density of oxide surface defects and vacancies being involved, this wetting anyhow remains incomplete and leaves the underlying surface partially uncovered. The smaller area imaged in **Figure 3(c)** provides clearer insights about the MgO morphology, especially with two relevant characteristics. First of all, while we were expecting an oxide film continuity mainly disrupted by defects, dot-shaped MgO protrusions can be solved here as regular surface modulations induced within the film. This phenomenon was attributed to the appearance of a Moiré structure. Then, a large part of these oxide dots adopt a conformation in rows running towards well defined directions of the surface, even though many regions remain widely disordered. While too local for inducing a significant diffraction pattern with LEED, nevertheless, we interpret the observed surface ordering as a strong indicator of MgO crystalline domain formation.

Figure 4(a) presents a $65 \times 40 \text{ nm}^2$ area of the annealed oxide that was probed at higher STM resolution, showing more clearly the local order established in the MgO ML film. Despite numerous disordered regions (e.g. oxide rows randomly oriented, holes or surface vacancies), two perpendicular directions can be noticed as preferential ones for the growth of MgO protrusions. Both oxide rows directions are measured at 45° disoriented with respect to the Ni(100) non-dense directions. We underline that the arrow labeled as Ni[001] in the image was oriented by analysis of the reciprocal space, keeping fixed the sample position between the LEED and the STM chamber.

A magnified view is given **Figure 4(b)**, showing MgO protrusions locally well-ordered within a $16 \times 16 \text{ nm}^2$ surface area. With regard to the regular growth of few oxide dotted rows in this region, it is obvious that the formation of a 2D pattern with the four-fold symmetry would greatly mirror such ordered distribution in the oxide domains. On the corresponding line profile of **Figure 4(c)** indeed, an average distance of 1.75 nm can be estimated between adjacent MgO protrusions along oxide row direction. Finally, this measure matches well the value of 1.68 nm corresponding to $4 \times a(\text{MgO})$ lattice parameter.

Considering the above, we assume the (100)-oriented epitaxy of 1 MgO ML on Ni(100) as likely source of the surface-induced modulations evidenced with STM. For further supporting this experimental study, an epitaxial model of 1 MgO(100) plane being 45° rotated with respect to the Ni(100) surface was then proposed as a crystallization path for the oxide film.

The ball model shown on **Figure 5** was therefore sketched for investigating, through the modeling of the Moiré pattern observed **Figure 4(b)**, the epitaxial relationship between the Ni(100) substrate and the MgO ML film. Two crystalline lattices of Ni(100) and MgO(100) planes were stacked, looking for the most suitable configuration. Note that Ni crystallizes as a fcc structure with a lattice parameter of 3.52 \AA , while MgO has a typical NaCl structure with a lattice parameter of 4.21 \AA . When considering the (100) orientation in the Ni crystal, the

densest direction is the Ni[011]. When looking at the crystalline structure of MgO material, the densest directions are equivalent to the MgO[100]. As Ni is defined here as bulk substrate, we assume the oxide ML will adapt its lattice to the underlying Ni plane, so that the MgO lattice parameter should slightly expand during the oxide crystallization. Interestingly, characteristic Moiré modulations arise in surface as soon as the Ni[011] and MgO[010] densest directions are set parallel, assuming that a tensile strain of 3% is applied through the MgO(100) plane. Also, the corresponding Moiré structure depicts a regular square motif with a typical length of 1.74 nm. In such epitaxial model, we observe a coincidence lattice matching relying on a ratio of 4 (MgO) : 7 (Ni) between the surface unit cells that belong to the expanded-MgO(100) and the Ni(100) respectively. On this basis, a square-shaped oxide super-lattice matching the substrate atoms every 4 MgO units would substantiate well both the ordering and characteristic spacing that were measured between the adjacent MgO protrusions. While allowing 3 % expansion of its lattice parameter finally, the MgO(100) plane would drastically reduce down to 0.46 % the in-plane mismatch remaining in the 4 (MgO) : 7 (Ni) super-lattice. According to these facts, we assume the proposed model accurately reflects the local Moiré structure that was probed experimentally on Figure 4(b) as a strong insight of MgO epitaxy. A route towards the MgO ML crystallization should therefore be built on Ni, even locally and following the epitaxial relationship we identified as [010] MgO(100) // [011] Ni(100).

This experimental work focused on exploring the first insights of epitaxial growth in the MgO ML / Ni(100) system. An atomically thick MgO film of stable stoichiometry and amorphous characteristics was firstly grown on Ni(100) at RT, using alternate phases of Mg atomic ML adsorption and O₂ soft exposure. The thermal treatment of this amorphous layer at 720 K under UHV enabled to produce afterwards a textured MgO film of (100)-oriented domains, ordered at a nanometer scale while disrupted by oxide structural defects. We evidenced the formation of a related Moiré super-structure, whose square shape and typical lengths were further investigated under combined STM observation and atomic modeling. While studying the Moiré structure in terms of lattice symmetry and preferential epitaxial directions, the crystallization path involved at the origin of MgO domain ordering could finally be solved as [010] MgO(100) // [011] Ni(100). This MgO super-lattice could be envisioned as a patterned template for further deposition of organic and inorganic materials. In search of novel spintronic applications of high performances, this study can also provide interesting prospects regarding the controlled epitaxy of tunnel oxide ultrathin films on ferromagnetic substrates.

The authors gratefully thank B. Aufray and H. Nguyen Thi for fruitful discussions and their generosity having contributed to optimize the experimental system dedicated to this study.

¹ G. Pacchioni and H. Freund, Chem. Rev. **113**, 4035 (2013).

² C.T. Campbell, Surf. Sci. Rep. **27**, 1 (1997).

³ X. Liu, C. Chen, Y. Zhao, and B. Jia, J. Nanomater. **2013**, (2013).

⁴ W. de Gruyter, editor, *Superconducting Quantum Interference Devices and Their Applications* (1985).

⁵ D. Panda and T.-Y. Tseng, Thin Solid Films **531**, 1 (2013).

⁶ G. Pacchioni, Chem. - A Eur. J. **18**, 10144 (2012).

⁷ L. Giordano and G. Pacchioni, Acc. Chem. Res. **44**, 1244 (2011).

⁸ S.A. Chambers, Adv. Mater. **22**, 219 (2010).

- ⁹ C.J. Nelin, P.S. Bagus, M.A. Brown, M. Sterrer, and H.J. Freund, *Angew. Chemie - Int. Ed.* **50**, 10174 (2011).
- ¹⁰ C. Freysoldt, P. Rinke, and M. Scheffler, *Phys. Rev. Lett.* **99**, 1 (2007).
- ¹¹ H.J. Freund, *Faraday Discuss.* **114**, 1 (1999).
- ¹² F.P. Netzer, F. Allegretti, and S. Surnev, *J. Vac. Sci. Technol. B* **28**, 1 (2010).
- ¹³ T. Jaouen, S. Tricot, G. Delhaye, B. L??pine, D. S??billeau, G. J??z??quel, and P. Schieffer, *Phys. Rev. Lett.* **111**, 1 (2013).
- ¹⁴ C. Tusche, H.L. Meyerheim, N. Jedrecy, G. Renaud, A. Ernst, J. Henk, P. Bruno, and J. Kirschner, *Phys. Rev. Lett.* **95**, 1 (2005).
- ¹⁵ F. Greullet, C. Tiusan, F. Montaigne, M. Hehn, D. Halley, O. Bengone, M. Bowen, and W. Weber, *Phys. Rev. Lett.* **187202**, 5 (2007).
- ¹⁶ P. Mavropoulos, N. Papanikolaou, and P.H. Dederichs, *Phys. Rev. Lett.* **6** (2000).
- ¹⁷ S.S.P. Parkin, C. Kaiser, A. Panchula, P.M. Rice, B. Hughes, M. Samant, and S. Yang, *Nature Materials* **3**, 2 (2004).
- ¹⁸ J. Mathon and A. Umerski, *Phys. Rev. B.* **63**, 1 (2001).
- ¹⁹ J. Pal, M. Smerieri, E. Celasco, L. Savio, L. Vattuone, and M. Rocca, *Phys. Rev. Lett.* **112**, 1 (2013).
- ²⁰ D.F. F?rster, J. Klinkhammer, C. Busse, S.G. Altendorf, T. Michely, Z. Hu, Y.Y. Chin, L.H. Tjeng, J. Coraux, and D. Bourgault, *Phys. Rev. B - Condens. Matter Mater. Phys.* **83**, 1 (2011).
- ²¹ N. Doudin, S. Pomp, M. Blatnik, R. Resel, M. Vorokhta, J. Goniakowski, C. Noguera, F.P. Netzer, and S. Surnev, *Surf. Sci.* **659**, 20 (2017).
- ²² M.G. Jeong, S.Y. Kim, D.H. Kim, S.W. Han, I.H. Kim, M. Lee, Y.K. Hwang, and Y.D. Kim, *Appl. Catal. A Gen.* **515**, 45 (2016).
- ²³ S. Vizzini, H. Oughaddou, J.Y. Hoarau, J.P. Bib??rian, and B. Aufray, *Appl. Phys. Lett.* **95**, 3 (2009).
- ²⁴ S. Vizzini, H. Oughaddou, C. L??andri, V.K. Lazarov, A. Kohn, K. Nguyen, C. Coudreau, J.P. Bib??rian, B. Ealet, J.L. Lazzari, F. Arnaud d'Avitaya, and B. Aufray, *J. Cryst. Growth* **305**, 26 (2007).
- ²⁵ B. Sarpi, N. Rochdi, R. Daineche, M. Bertoglio, C. Girardeaux, A. Baronnet, J. Perrin-Toinin, M. Bocquet, M. Djafari Rouhani, A. Hemeryck, and S. Vizzini, *Surf. Sci.* **642**, L1 (2015).
- ²⁶ B. Sarpi, R. Daineche, C. Girardeaux, A. Hemeryck, and S. Vizzini, *Appl. Surf. Sci.* **361**, 259 (2016).
- ²⁷ B. Sarpi, R. Daineche, C. Girardeaux, M. Bertoglio, F. Derivaux, J.P. Biberian, A. Hemeryck, and S. Vizzini, *Appl. Phys. Lett.* **106**, (2015).
- ²⁸ A.M. Baro, M. Salmeron, and J.M. Rojo, *J. Phys. F Met. Phys.* **5**, 826 (1975).
- ²⁹ B. Sarpi, N. Rochdi, R. Daineche, M. Bertoglio, C. Girardeaux, A. Baronnet, J. Perrin-Toinin, M. Bocquet, M. Djafari Rouhani, A. Hemeryck, and S. Vizzini, *Surf. Sci.* **642**, L1 (2015).
- ³⁰ F.C. Frank and J.H. van der Merwe, *Proc. R. Soc. A Math. Phys. Eng. Sci.* **198**, 205 (1949).
- ³¹ A. Barbier, *Surf. Sci.* **406**, 69 (1998).
- ³² M.P. Seah, *J. Phys. F Met. Phys.* **3**, 1538 (1973).
- ³³ E. Clementi, D.L. Raimondi, and W.P. Reinhardt, *J. Chem. Phys.* **47**, 1300 (1967).
- ³⁴ M.K. Bernett, J.S. Murday, and N.H. Turner, **12**, 375 (1977).
- ³⁵ K.D. Childs, B.A. Carlson, L.A. LaVanier, J.F. Moulder, D.F. Paul, W.F. Stickle, and D.G. Watson, *Handbook of Auger Electron Spectroscopy: A Reference Book of Standard Data for Identification and Interpretation of Auger Electron Spectroscopy Data*, 2nd ed. Pe (1996).

Figure captions

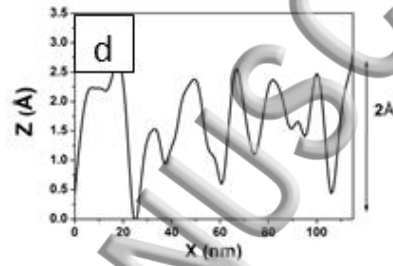
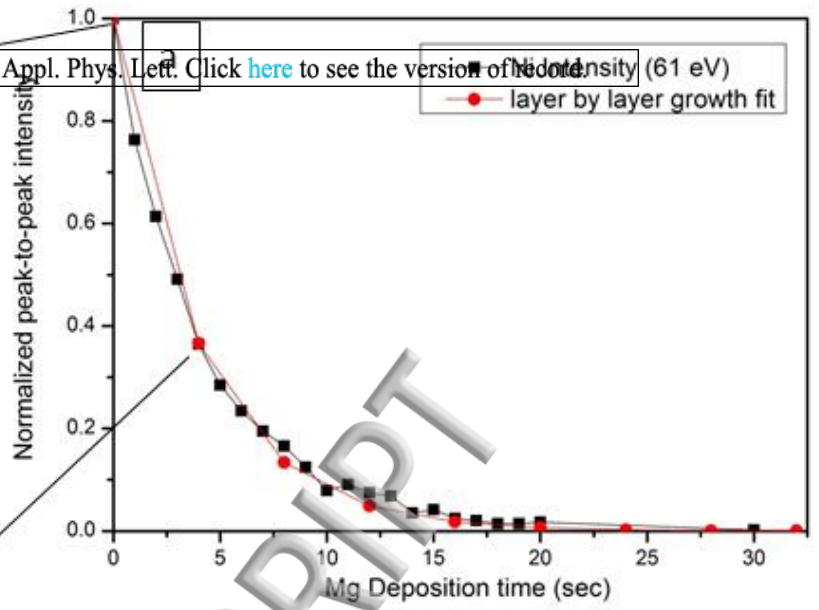
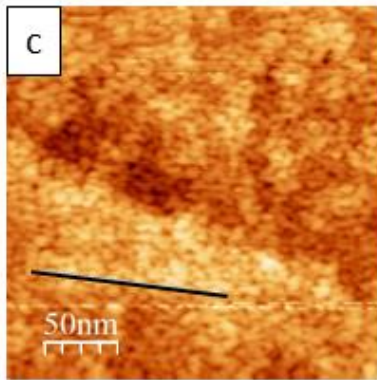
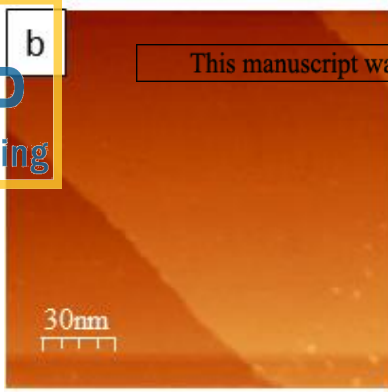
Fig. 1 (a): Peak-to-peak Auger signal of the Ni(100) substrate, monitored as a function of Mg deposition time at RT (black squared line). The theoretical plot (red dotted line) fits a layer-by-layer growth mode. **(b):** 150 x 150nm² filled-states STM image ($U=0.3V$, $I=3nA$) of the bare Ni(100) surface. **(c):** 250 x 250 nm² empty-states STM image ($U=-0.3V$, $I=1.5nA$) of 1 Mg monolayer deposited on Ni (100). The line scan drawn in **(d)** depicts corrugation of the corresponding line in (c).

Fig. 2: AES spectra recorded while keeping constant the emission current at each step of the oxide growth process. (a) Bare Ni (100) substrate; (b) one Mg ML deposited at RT; (c) one MgO ML oxidized at RT and (d) 1 MgO ML annealed at 720 K for few minutes under UHV.

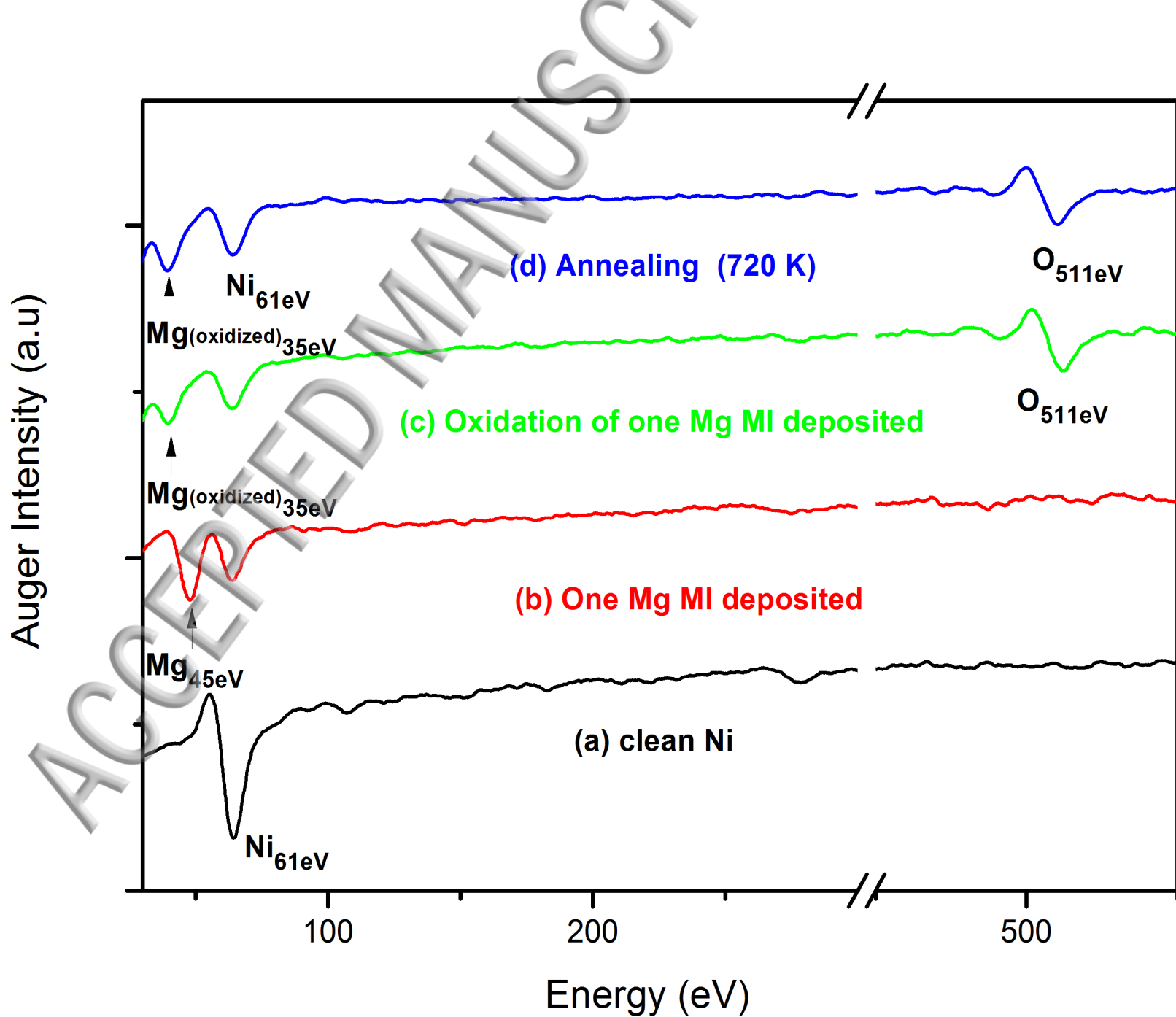
Fig.3 (a): 400 x 400nm² STM image of the bare Ni substrate. **(b):** 400 x 400nm² filled-states STM image ($U=2.2V$, $I=0.5nA$) of a nearby sample region probed after deposition of 1 MgO monolayer and annealing at 720 K. **(c):** 150 x 150nm² STM image recorded under the same tunneling conditions as (b), showing locally ordered MgO protusions characteristic of a Moiré structure.

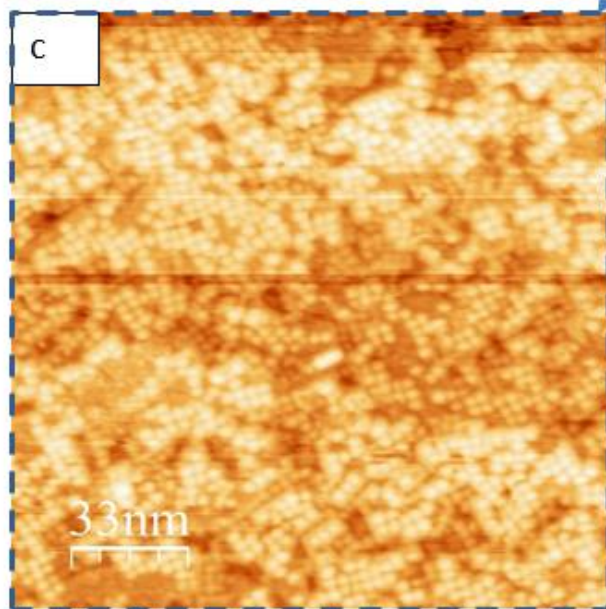
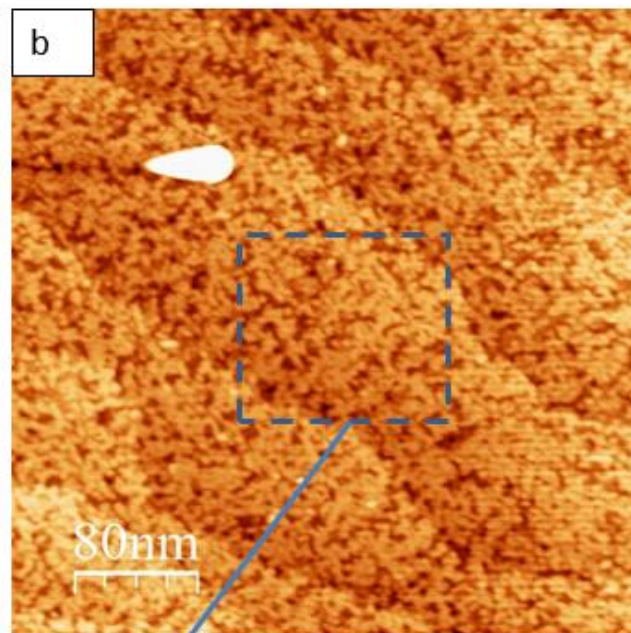
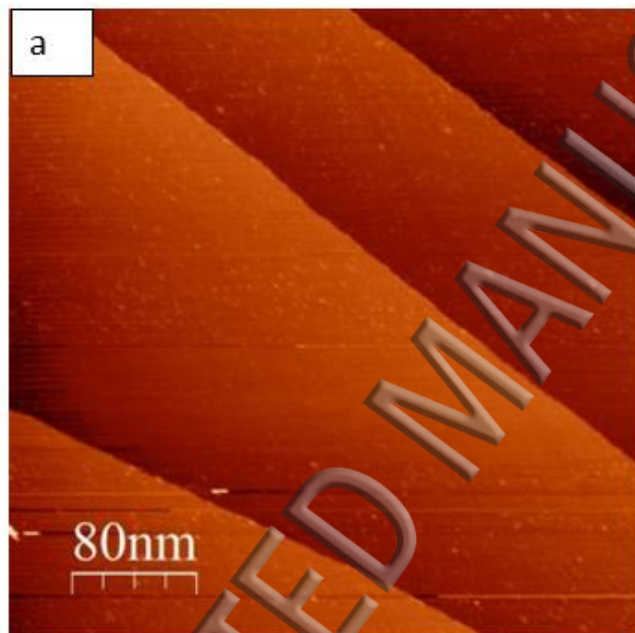
Fig.4 (a): 65 x 40nm² filled-states STM image ($U=1.7V$, $I=0.3nA$) showing MgO domains locally ordered in dotted lines running towards two perpendicular directions of growth (grey stripes), 45° disoriented with respect to the substrate non-dense Ni[001] (or equivalent) direction. **(b):** 16 x 16nm² magnified image of the inset area drawn in (a), recorded under the same tunneling conditions as (a). **(c):** Line scan corresponding to the square-shaped Moiré structure shown in (b), plotted along oxide row direction (see labels).

Fig. 5: Ball model of one MgO (100) plan stacked on the Ni(100) surface plan, showing a coincidence lattice matching when the MgO[010] and Ni[011] densest directions are set parallel. In strong agreement with our experimental observations, a Moiré structure of square symmetry and 1.74 nm typical length emerges from this epitaxial configuration.



ACCEPTED MANUSCRIPT





Ni [001]

Oxide rows direction

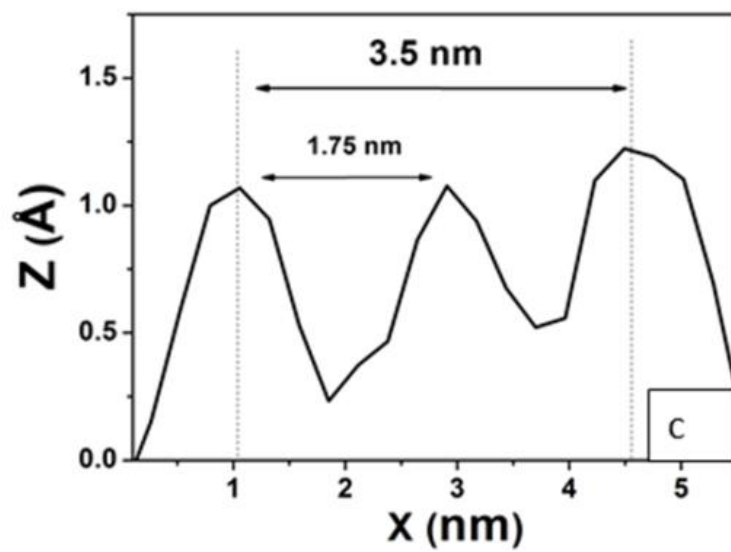
45°

10nm

a

2.2nm

b



● Ni ● Mg ● O

